Anomalous photon-assisted tunneling in periodically driven Majorana nanowires and BCS charge measurement

Yuchen Zhuang [1,2] and Qing-Feng Sun [1,2,3,*]

[1] *International Center for Quantum Materials, School of Physics, Peking University, Beijing 100871, China*
[2] *CAS Center for Excellence in Topological Quantum Computation, University of Chinese Academy of Sciences, Beijing 100190, China*
[3] *Beijing Academy of Quantum Information Sciences, West Bld.#3, No.10 Xibeiwang East Rd., Haidian District, Beijing 100193, China*

(Received 30 July 2021; revised 19 January 2022; accepted 8 April 2022; published 26 April 2022)

The photon-assisted tunneling of Majorana bound states in a Majorana nanowire driven by the periodic field is studied both theoretically and numerically. We find that Majorana bound states exhibit an anomalous photon-assisted tunneling signal, which is different from an ordinary fermionic state: the height of photonic sidebands is related to the degree of Majorana nonlocality. Moreover, we show that the Bardeen—Cooper—Schrieffer (BCS) charge and spin components of subgap states can be well revealed by the local conductance. Our work illuminates the effect of driving field on Majorana bound states and provides a systematic scheme to directly measure BCS information of overlapping Majorana bound states.

DOI: 10.1103/PhysRevB.105.165148

I. INTRODUCTION

A Majorana bound state (MBS) is a chargeless quasiparticle whose antiparticle is equal to itself [1–4]. It has attracted a widespread attention for a long time because of its potential applications in fault-tolerant quantum computations [5–7]. One way to prepare MBSs is based on an one-dimensional (1D) hybrid superconducting-semiconducting nanowire in the presence of spin-orbit coupling and Zeeman splitting (often dubbed as the Majorana nanowire) [8–10]. MBSs can lead to a series of novel transport phenomena, such as a quantized zero bias conductance peak (ZBCP) with a value of $2e^2/h$ through the resonant Andreev reflection [11], fractional Josephson effect [2,12], and spin-selective equal-spin Andreev reflection [13].

Although an isolated zero-energy MBS has no charge and spin [14], when two MBSs are coupled (i.e., the Majorana nanowire's length L is not longer than the Majorana decay length ξ_M), a nonzero energy state with nonquantized charge [Bardeen-Cooper-Schrieffer (BCS) charge] and spin will be generated [15–17]. This finite BCS charge is related to the nonlocality of MBSs [18–20], which is of particular significance to implement a topological qubit [19]. Recently, both theory and experiment demonstrated that a three-terminal setup can be used to extract the local BCS charge of bound states close to the ends of the wire [21,22]. However, a systematic scheme to measure this BCS charge (e.g., measure its spin and spatial information) is still lacking.

Periodically driven systems have been of concern for a long time [23,24]. One of the key features is that electrons tunneling through these systems can absorb or emit multiple photons, causing photonic sideband peaks at harmonics in the conductance-voltage curves, which is known as photon-assisted tunneling (PAT). The study of this phenomenon can trace back to the early pioneering work by Tien and Gordon in superconductor-insulator-superconductor films [25]. They raise a simple relation that the nth PAT peaks is modulated by a square of Bessel function $J_n^2(eV_f/\hbar\omega)$ [26]. Here e is the charge of the electron, $\hbar\omega$ is the photon's energy, and V_f is the driving amplitude. Until now, periodically driving physics has been explored in a widespread range including quantum dots [27,28], the semiconductor superlattice [29], as well as two-dimensional electron gas [30–32].

The interplay between PAT and MBSs in the topological superconductor also raises recent common interest. One recent work studied the PAT from ac-driven normal electrodes into the Majorana nanowire with MBSs and find resulting nonzero sideband peaks [33]. Another recent work analyzed the photon-assisted resonant Andreev reflection from ac-driven superconducting tips or normal electrodes into subgap states like Yu-Shiba-Rusinov (YSR) states and MBSs, and argue that it could provide a high-accuracy method to measure small but nonzero energies of subgap states [34]. But essentially, these previous studies focused on a case that complete fermions were driven to absorb and emit photons tunneling into the subgap states in superconducting system. But how MBS, as a "half fermion," responds under the periodically driving field is still an open question. Moreover, since the PAT signal is directly connected with the charge in the tunneling process, we can naturally wonder whether PAT could give us the BCS charge information of bound states.

The goal of this paper is to study the PAT signals of MBSs in the periodically driven Majorana nanowire connected by two normal leads, in proximity to an equilibrium superconductor, as shown in Fig. 1(a). Both numerically and analytically, our results illuminate that MBSs show an anomalous PAT signal different from an ordinary fermionic state in Fig. 1(b): photonic sideband peaks disappear when MBSs

*sunqf@pku.edu.cn

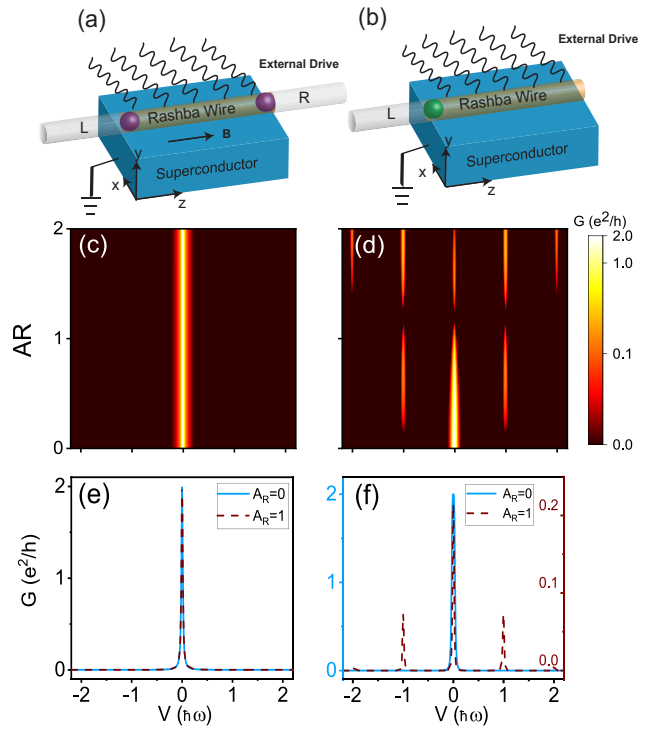

FIG. 1. (a, b) Schematic representation for (a) MBSs and (b) single impurity in periodically driven nanowire, which is in the proximity to the grounded superconductor. (a) Two MBSs (purple dots) located at the two ends of the 1D Majorana nanowire, which is connected to two normal leads. (b) A trivial impurity (green dot) lies between the normal left lead and the semiconductor nanowire. (c)–(f) Time-averaged local conductance G as functions of bias V and relative driving field strength A_R for the (c, e) MBSs and (d, f) for the trivial impurity. Here nanowire length $N = 700$, static magnetic field $V_0 = 400\,\mu$eV, chemical potential $\mu = 0$, the photon energy $\hbar\omega = 20\,\mu$eV, corresponding to frequency $f \approx 5$ GHz. Other parameters are given in the text.

are well separated but reappear once MBSs are coupled. This phenomenon is attributed to the charge-neutral and spinless properties of Majorana fermions. We further prove that the height of PAT peaks is relevant to the BCS charge of subgap states. Based on this, we propose a method to directly extract both BCS charge and spin components of overlapping MBSs via the local conductance.

The rest of this paper is organized as follows. In Sec. II, we give our model and present a low-energy effective model to describe the MBSs under the periodically driving field. In Sec. III, we use the nonequilibrium Green's function method to calculate current and conductance. We also conduct some numerical calculations for MBSs and trivial Andreev bound states (ABSs) induced by hybridized impurity, respectively, and further compare their results. In Sec. IV, we analyze the time-averaged conductance of overlapping Majoranas and point out one way to extract their BCS charge. In Sec. V, we consider a case where microwave field and harmonic magnetic field coexist and discuss how to extract the BCS spin information along any direction. We put the summary and some discussions in Sec. VI. Some detailed calculations and supplementary figures are all concluded in Appendices A to C.

II. MODEL AND HAMILTONIAN

A. Model for periodically driven Majorana nanowire and single impurity

Specifically, to describe the 1D Majorana nanowires as shown in Fig. 1(a), the Bogoliubov–de Gennes (BdG) Hamiltonian in the Nambu basis $\{\psi_\uparrow(z), \psi_\downarrow(z), \psi_\uparrow^\dagger(z), \psi_\downarrow^\dagger(z)\}$ can be written as [8,9]

$$H_{nw}^{\mathrm{BdG}} = \left(\frac{p_z^2}{2m^*} - \mu + V_0\sigma^z + \alpha_R p_z \sigma^y\right)\tau^z - \widetilde{\Delta}\sigma^y\tau^y, \quad (1)$$

where Pauli matrices σ and τ act on the spin and particle-hole space. m^* is the effective electronic mass. α_R and $V_0 = g\mu_B B/2$ are the spin-orbit coupling strength and the static Zeeman field with landé g-factor and magnetic field B, μ and $\tilde{\Delta}$ represent the chemical potential and proximity-induced pairing potential. To facilitate numerical calculations, we discretize this Hamiltonian into tight-binding form and also include the periodically driving field and coupling between the left and right leads

$$H_{\mathrm{MBS}}(t) = H_{nw} + H_{fm}(t) + H_{T1} + H_L + H_R, \quad (2)$$

where

$$\begin{aligned} H_{nw} = &\sum_{i=1,s}^{N}(2t_N - \mu)c_{is}^\dagger c_{is} - \sum_{i=1,s}^{N-1} t_N(c_{is}^\dagger c_{i+1,s} + \mathrm{H.c.}) \\ &- \sum_{i=1,s,s'}^{N-1}\left[\frac{\alpha_R}{2a}c_{is}^\dagger(i\sigma^y)_{ss'}c_{i+1,s'} + \mathrm{H.c.}\right] \\ &+ \sum_{i=1,s,s'}^{N} V_0 c_{is}^\dagger(\sigma^z)_{ss'}c_{is'} + \sum_{i=1}^{N}(\widetilde{\Delta}c_{i\uparrow}^\dagger c_{i\downarrow}^\dagger + \mathrm{H.c.}) \end{aligned} \quad (3)$$

and

$$\begin{aligned} H_{fm}(t) &= \sum_{i,s} A\cos(\omega t)c_{is}^\dagger c_{is}, \\ H_{\alpha=L/R} &= \sum_{k\alpha,s}\varepsilon_{k\alpha}a_{k\alpha s}^\dagger a_{k\alpha s}, \\ H_{T1} &= \sum_{kL,s} t_L c_{1s}^\dagger a_{kLs} + \sum_{kRs} t_R c_{Ns}^\dagger a_{kRs} + \mathrm{H.c.} \end{aligned} \quad (4)$$

Here i and s ($s = \uparrow, \downarrow$ or ± 1) label the lattice coordinate and the spin index, N and a are the number of lattice points and the lattice constant of the Majorana nanowire, t_N is the nearest hopping energy. H_{fm} describes the microwave driving field with the driving amplitude A. Besides the microwave field, the harmonic magnetic field along the z direction is also investigated in our following calculations with $H_{fz}(t) = \sum_{i,s,s'} A\cos(\omega t)(\sigma^z)_{ss'}c_{is}^\dagger c_{is'}$. $H_{\alpha=L/R}$ describes the left/right normal leads ($t_{L,R}$ can be set as real). H_{T1} is the tunneling Hamiltonian between central Majorana nanowires and the left/right leads. For simplicity, we made some assumptions. (i) The external harmonic field is only applied on the 1D Majorana nanowire and does not affect other parts [35,36]. (ii) The frequency of the external field is much lower than $\tilde{\Delta}$ and the adiabatic approximation holds, thus the harmonic field only changes the single electron energy [37–39]. In fact, even

if the frequency reaches to 10 GHz, the energy $\hbar\omega$ is about 40 μeV. This is usually much smaller than $\tilde{\Delta}$ which is around 200 μeV.

To compare the MBS with an ordinary fermionic state, we consider another simple case where an impurity is hybridized with the superconductor [Fig. 1(b)]. These kinds of ABSs can be described by the impurity Hamiltonian [40]

$$H_{\rm ABS} = H_d + H_{sc} + H_{T2} + H_L + H_{fm}(t), \tag{5}$$

where

$$\begin{aligned} H_d &= \sum_s E_0 d_s^\dagger d_s, \\ H_{sc} &= \sum_{k,s} \varepsilon_{sc,k} b_{ks}^\dagger b_{ks} + \sum_k \tilde{\Delta} b_{k\uparrow}^\dagger b_{-k\downarrow}^\dagger + \text{H.c.}, \\ H_{fm}(t) &= \sum_s A\cos(wt) d_s^\dagger d_s, \\ H_{T2} &= \sum_{ks} t_L d_s^\dagger a_{kLs} + t_{sc} d_s^\dagger b_{ks} + \text{H.c.} \end{aligned} \tag{6}$$

Here H_d is the impurity Hamiltonian. H_{sc} is the grounded s-wave superconductor Hamiltonian. H_{fm} and H_{T2} is for the microwave driving field and tunneling part, respectively (H_{fz} is also included in the following). The Hamiltonian H_L for the normal left lead are the same as the first case. Based on the intrinsic superconducting limit and wide-band limit [36,41], the superconductor reservoir can be integrated out to introduce a self-energy term $\mathbf{\Sigma}_{sc}^r = -\frac{\widetilde{\Gamma}^{sc}}{2} d_\uparrow^\dagger d_\downarrow^\dagger + \text{H.c.}$ with $\widetilde{\Gamma}^{sc} = 2\pi\rho_s|t_{sc}|^2$ (ρ_s is the superconducting density of states) [36,40]. Similarly, the couplings between the Majorana nanowire and the normal leads can also introduce a self-energy term $\Sigma_{L,ij,lr}^r = -i\frac{\widetilde{\Gamma}^L}{2}\delta_{ij}\delta_{j1}\delta_{lr}$ and $\Sigma_{R,ij,lr}^r = -i\frac{\widetilde{\Gamma}^R}{2}\delta_{ij}\delta_{jN}\delta_{lr}$ with $\widetilde{\Gamma}^{\alpha=L,R} = 2\pi\rho_\alpha|t_\alpha|^2$ (ρ_α is the density of states in the normal lead α). Here the first two indices denote sites and the other two indices denote the Nambu spinor.

B. Projected Hamiltonian and BCS charge

To analytically investigate how the MBSs are affected by microwave driving field, by the Bogoliubov transformation $\psi_n^\dagger = \sum_{i,s} u_{is}^{(n)} c_{is}^\dagger + v_{is}^{(n)} c_{is}$, the Majorana nanowire Hamiltonian H_{nm} in Eq. (3) can be diagonalized as

$$H_{nw} = \sum_n \varepsilon_n \psi_n^\dagger \psi_n, \tag{7}$$

where $u_{is}^{(n)}$, $v_{is}^{(n)}$ are the particle and hole components of the ε_n eigenstate at the site i with spin s. In view of the fact that the energy of concerned subgap states and driving field frequency ω are both much lower than the induced topological gap, the mix between subgap states and quasiparticle continuum could be ignored. Hence, we can just focus on the projected Hamiltonians of Majorana nanowire and harmonic field, $H^p = H_{nm}^p + H_{fm/z}^p$, in the space formed by the lowest-energy subgap state $(\psi_0^\dagger, \psi_0)$ with energy ϵ_0:

$$\begin{aligned} P &= \begin{pmatrix} u_{1\uparrow}^{(0)*} & u_{1\downarrow}^{(0)*} & v_{1\uparrow}^{(0)*} & v_{1\downarrow}^{(0)*} \cdots & u_{N\uparrow}^{(0)*} & u_{N\downarrow}^{(0)*} & v_{N\uparrow}^{(0)*} & v_{N\downarrow}^{(0)*} \\ v_{1\uparrow}^{(0)} & v_{1\downarrow}^{(0)} & u_{1\uparrow}^{(0)} & u_{1\downarrow}^{(0)} \cdots & v_{N\uparrow}^{(0)} & v_{N\downarrow}^{(0)} & u_{N\uparrow}^{(0)} & u_{N\downarrow}^{(0)} \end{pmatrix}, \\ H_{nw}^p &= PH_{nw}P^\dagger = \begin{pmatrix} \varepsilon_0 & 0 \\ 0 & -\varepsilon_0 \end{pmatrix}, \\ H_{fm}^p &= PH_{fm}P^\dagger = \begin{pmatrix} QA\cos(wt) & 0 \\ 0 & -QA\cos(wt) \end{pmatrix}, \\ H_{fz}^p &= PH_{fz}P^\dagger = \begin{pmatrix} \zeta_z A\cos(\omega t) & 0 \\ 0 & -\zeta_z A\cos(\omega t) \end{pmatrix}. \end{aligned} \tag{8}$$

P is the projection operator on the lowest-energy states. Q and ζ_z is the BCS charge and BCS spin polarization along the z direction for the quasiparticle state $\psi_0^\dagger$:

$$\begin{aligned} Q &= \sum_{i,s} \left(|u_{is}^{(0)}|^2 - |v_{is}^{(0)}|^2\right), \\ \zeta_z &= \sum_{i,s} s\left(|u_{is}^{(0)}|^2 - |v_{is}^{(0)}|^2\right). \end{aligned} \tag{9}$$

In the continuum space, Q or ζ could be generalized as $Q = \sum_s \int (|u_s^{(0)}(z)|^2 - |v_s^{(0)}(z)|^2)\, dz$ or $\zeta_z = \sum_s s \int (|u_s^{(0)}(z)|^2 - |v_s^{(0)}(z)|^2)\, dz$. Equation (8) reveals a fact: the external driving field on the lowest-energy state of H_{nm} in our case should be renormalized by a factor, corresponding to the BCS charge Q (or BCS spin polarization ζ_z). It's natural in view of the quasiparticles interacting with external fields with charge Qe rather than e as electrons. For further analysis, we also define its magnitude as

$$Q_{\rm BCS} = \left|\sum_{i,s}\left(|u_{is}^{(0)}|^2 - |v_{is}^{(0)}|^2\right)\right| \tag{10}$$

and BCS spin component magnitude as

$$Q_{{\rm BCS},s} = \left|\sum_{i}\left(|u_{is}^{(0)}|^2 - |v_{is}^{(0)}|^2\right)\right|. \tag{11}$$

$Q_{\rm BCS}$ here is parallel to the definition of δN introduced in Refs. [16,20]. Its value ranges from 0 to 1.

It is easy to find that $Q = 0$ and $\zeta_z = 0$ as long as $\psi^\dagger = \psi$, which echoes Majoranas' charge-neutral and spinless properties. Thus, isolated MBS itself should not be affected by the driving field. For a sufficiently long 1D Majorana nanowire in topological region, the lowest-energy states are nonlocal states formed by two well-separated MBSs at the ends of the wire, with zero BCS charge. As a result, PAT signals must disappear in this case. In contrast, the fermionic trivial ABSs are usually charged, even though their energy crosses zero. PAT signals for them should be observed.

The deeper meaning of the BCS charge is related to the Majorana nonlocality [18–20]. This can be proved as follows. For any zero-energy ABS, regardless of its topological origin,

can always be decomposed into two MBSs:

$$\gamma_1 = \psi_0^\dagger + \psi_0, \quad \gamma_2 = i(\psi_0^\dagger - \psi_0). \tag{12}$$

The spatial wave function of MBS can be written as $\gamma_i = \sum_{j,s} \Phi_{js}^{(\gamma_i)} c_{js}^\dagger + (\Phi_{js}^{(\gamma_i)})^* c_{js}$, with

$$\begin{aligned} \Phi_{js}^{\gamma_1} &= u_{js}^{(0)} + \left(v_{js}^{(0)}\right)^*, \\ \Phi_{js}^{\gamma_2} &= i\left[u_{js}^{(0)} - \left(v_{js}^{(0)}\right)^*\right]. \end{aligned} \tag{13}$$

Without lose of generality, $u_{is}^{(0)}$ and $v_{is}^{(0)}$ can be set as real and BCS charge magnitude in Eq. (10) could be regulated as overlap between MBSs' wave functions

$$Q_{\mathrm{BCS}} = \left| \sum_{js} \Phi_{js}^{\gamma_1} * \Phi_{js}^{\gamma_2} \right|. \tag{14}$$

Trivial ABSs are composed of two highly overlapping or partially separated MBSs with finite BCS charge. Usually, when MBSs are spatially separated (e.g., topological MBSs located at two ends of the nanowire) or spin-separated (e.g., quasi-MBSs originating from two spin channels [42,43]), BCS charge in Eq. (14) can approach zero within a large parameter range. This kind of well-separated MBSs have potential value in (parametric) non-Abelian braiding [43,44]. We reveal that BCS charge information of overlapping MBSs can naturally appear in Eq. (8). This is one of our main findings.

III. CURRENTS AND CONDUCTANCE UNDER PERIODICALLY DRIVING FIELD

To demonstrate our argument in Sec. II. In this section, we try to derive the current and conductance in detail for periodically driven nanowires and impurity by using the nonequilibrium Green's function method [37–39,41]. Along with Floquet-Landauer formalism [45–47], numerical results are also performed.

A. Derivation of current and conductance

Assuming the bias voltage is only applied on the left lead with $V_L = V$ and the others are connected to the ground. The current flowing from the normal left lead into the periodically driven Majorana nanowire via the time derivative of electron number operator ($N_L = \sum_{k,s} a_{kL,s}^\dagger a_{kL,s}$) is [37,39]

$$I_L(t) = -e\langle \dot{N}_L \rangle = 2e\mathrm{Re}\left\{ \sum_{k,l(l=1,2)} t_L G_{1kL,ll}^<(t,t) \right\}. \tag{15}$$

Here the Green's functions $\mathbf{G}^<, \mathbf{G}^r$ are defined in the four-component Nambu basis as

$$\begin{aligned} \mathbf{G}_{ij}^<(t,t') &\equiv i\left\langle \begin{pmatrix} c_{j\uparrow}^\dagger(t') \\ c_{j\downarrow}^\dagger(t') \\ c_{j\uparrow}(t') \\ c_{j\downarrow}(t') \end{pmatrix} \left(c_{i\uparrow}(t), \quad c_{i\downarrow}(t), \quad c_{i\uparrow}^\dagger(t), \quad c_{i\downarrow}^\dagger(t)\right) \right\rangle, \\ \mathbf{G}_{ij}^r(t,t') &\equiv -i\theta(t-t')\left\langle \left\{ \begin{pmatrix} c_{i\uparrow}(t) \\ c_{i\downarrow}(t) \\ c_{i\uparrow}^\dagger(t) \\ c_{i\downarrow}^\dagger(t) \end{pmatrix} \right. \right. \\ &\quad \left. \left. \times \left(c_{j\uparrow}^\dagger(t'), \quad c_{j\downarrow}^\dagger(t'), \quad c_{j\uparrow}(t'), \quad c_{j\downarrow}(t')\right) \right\} \right\rangle, \end{aligned} \tag{16}$$

where i, j represent the index kL, kR in the normal leads, and site $1, 2, 3, \ldots, N$ in the Majorana nanowire. Using the Dyson equation [37,39] and wide-band limit [41], the current can be formulated as (in units of $\hbar = 1$)

$$\begin{aligned} I_L(t) = \sum_{l=1}^{2} \Bigg(& -2e \int_{-\infty}^{t} dt_1 \int \frac{d\varepsilon}{2\pi} \widetilde{\Gamma}^L f_L(\varepsilon) \\ & \mathrm{Im}\{e^{-i\varepsilon(t_1-t)} G_{11,ll}^r(t,t_1)\} - e\widetilde{\Gamma}^L \mathrm{Im}\left\{G_{11,ll}^<(t,t)\right\} \Bigg), \end{aligned} \tag{17}$$

with the first two subscripts of the Green's functions denoting sites and the second two subscripts denoting the Nambu spinor. We introduce level-width function matrices $(\mathbf{\Gamma}^L)_{ij,lr} = 2\pi\rho_L t_L^2 \delta_{ij}\delta_{j1}\delta_{lr} \equiv \widetilde{\Gamma}^L \delta_{ij}\delta_{j1}\delta_{lr}$ and $(\mathbf{\Gamma}^R)_{ij,lr} = 2\pi\rho_R t_R^2 \delta_{ij}\delta_{jN}\delta_{lr} \equiv \widetilde{\Gamma}^R \delta_{ij}\delta_{jN}\delta_{lr}$. To relate $\mathbf{G}^<$ and $\mathbf{G}^r$, using the Keldysh equation [41]

$$\mathbf{G}^<(t,t') = \int dt_1 \int dt_2 \mathbf{G}^r(t,t_1)\mathbf{\Sigma}^<(t_1,t_2)\mathbf{G}^a(t_2,t'). \tag{18}$$

Lesser self-energy due to the coupling between the left/right lead and the Majorana nanowire is $\mathbf{\Sigma}^<(t_1,t_2) = i\sum_{\alpha=L,R}\int \frac{d\varepsilon}{2\pi} e^{-i\varepsilon(t_1-t_2)} \mathbf{f}_\alpha(\varepsilon)\mathbf{\Gamma}^\alpha$ with $\mathbf{f}_\alpha(\varepsilon) = \mathrm{diag}[f_{\alpha e}(\varepsilon), f_{\alpha e}(\varepsilon), f_{\alpha h}(\varepsilon), f_{\alpha h}(\varepsilon)]$. $f_{\alpha e}(\varepsilon) = (e^{\frac{\varepsilon - eV_\alpha}{k_B T}} + 1)^{-1}$, and $f_{\alpha h}(\varepsilon) = (e^{\frac{\varepsilon + eV_\alpha}{k_B T}} + 1)^{-1}$ are Fermi-Dirac distributions of electrons and holes. Substituting Eq. (18) into Eq. (17), we can get the current

$$\begin{aligned} I_L(t) = \sum_{l=1}^{2} \Bigg\{ & -2e \int \frac{d\varepsilon}{2\pi} \widetilde{\Gamma}^L f_{Le}(\varepsilon)\, Im\left[\mathscr{A}_{11,ll}(\varepsilon,t)\right] - e(\widetilde{\Gamma}^L)^2 \int \frac{d\varepsilon}{2\pi} \left[f_{Le}(\varepsilon) \sum_{r=1}^{2} |\mathscr{A}_{11;lr}(\varepsilon,t)|^2 + f_{Lh}(\varepsilon) \sum_{r=3}^{4} |\mathscr{A}_{11;lr}(\varepsilon,t)|^2 \right] \\ & -e\widetilde{\Gamma}^L\widetilde{\Gamma}^R \int \frac{d\varepsilon}{2\pi} \left[f_{Re}(\varepsilon) \sum_{r=1}^{2} |\mathscr{A}_{1N;lr}(\varepsilon,t)|^2 + f_{Rh}(\varepsilon) \sum_{r=3}^{4} |\mathscr{A}_{1N;lr}(\varepsilon,t)|^2 \right] \Bigg\}. \end{aligned} \tag{19}$$

Notation $\mathscr{A}$ is defined as

$$\mathscr{A}(\varepsilon,t) = \int dt_1 \mathbf{G}^r(t,t_1)\, e^{i\varepsilon(t-t_1)}. \tag{20}$$

If the system is time independent, $\mathscr{A}$ actually refers to the Fourier transformation of the retarded Green's function $\mathbf{G}^r$. In the case of the time-periodic potential, we can refer to a Fourier transformation defined as [38,48]

$$\mathbf{G}(t,t_1)=\sum_n e^{in\omega t_1}\int\frac{d\varepsilon}{2\pi}e^{-i\varepsilon(t-t_1)}\mathbf{G}_n(\varepsilon). \tag{21}$$

We can also introduce the notation $\mathbf{G}_{mn}(\varepsilon)=\mathbf{G}_{n-m}(\varepsilon+m\omega)$ to relate different $\mathbf{G}_{mn}$ components. Then $\mathbf{G}_{mn}(\varepsilon)=\mathbf{G}_{0,n-m}(\varepsilon+m\omega)$. Under this transformation, the current in Eq. (19) can be reworded as

$$\begin{aligned}I_L(t)=\sum_{l=1}^{2}\Bigg\{&-2e\int\frac{d\varepsilon}{2\pi}\widetilde{\Gamma}^L f_{Le}(\varepsilon)Im\left[\sum_n e^{in\omega t}G^r_{11,ll;-n0}(\varepsilon)\right]\\&-e(\widetilde{\Gamma}^L)^2\int\frac{d\varepsilon}{2\pi}\left[f_{Le}(\varepsilon)\sum_{r=1}^{2}\left|\sum_n e^{in\omega t}G^r_{11,lr;-n0}(\varepsilon)\right|^2+f_{Lh}(\varepsilon)\sum_{r=3}^{4}\left|\sum_n e^{in\omega t}G^r_{11,lr;-n0}(\varepsilon)\right|^2\right]\\&-e\widetilde{\Gamma}^L\widetilde{\Gamma}^R\int\frac{d\varepsilon}{2\pi}\left[f_{\mathrm{Re}}(\varepsilon)\sum_{r=1}^{2}\left|\sum_n e^{in\omega t}G^r_{1N,lr;-n0}(\varepsilon)\right|^2+f_{Rh}(\varepsilon)\sum_{r=3}^{4}\left|\sum_n e^{in\omega t}G^r_{11,lr;-n0}(\varepsilon)\right|^2\right]\Bigg\}.\end{aligned} \tag{22}$$

We emphasize the last two subscripts in Eq. (22) refer to Fourier indices. Next, the time-averaged current or dc current over one period T ($T=2\pi/\omega$) can also be written as the Floquet-Landauer formalism [46,47,49]

$$\begin{aligned}&\langle I_L(t)\rangle\\&=\frac{1}{T}\int_0^T I(t)\,dt\\&=\sum_n\frac{e}{h}\int d\varepsilon\left\{\left(T^{(n)}_{\mathrm{ReLe}}(\varepsilon)+T^{(n)}_{\mathrm{RhLe}}(\varepsilon)+T^{(n)}_{\mathrm{LhLe}}(\varepsilon)\right)f_{Le}(\varepsilon)\right.\\&\quad\left.-T^{(n)}_{\mathrm{LeLh}}(\varepsilon)f_{Lh}(\varepsilon)-T^{(n)}_{\mathrm{LeRe}}(\varepsilon)f_{Re}(\varepsilon)-T^{(n)}_{\mathrm{LeRh}}(\varepsilon)f_{Rh}(\varepsilon)\right\}.\end{aligned} \tag{23}$$

The transmission coefficients are calculated by the retarded Green's function

$$T^{(n)}_{\alpha\beta,\alpha'\beta'}(\varepsilon)=Tr\left[\mathbf{\Gamma}^{\alpha}_{\beta}\mathbf{G}^{r,\beta\beta'}_{n0}(\varepsilon)\mathbf{\Gamma}^{\alpha'}_{\beta'}\mathbf{G}^{a,\beta'\beta}_{0n}(\varepsilon)\right]. \tag{24}$$

Here α,α' denote L,R normal leads and β,β' denote the electron e or hole h part. The resulting time-averaged differential conductance $G(V)=\frac{d\langle I_L(t)\rangle}{dV}$ in the low-temperature limit is

$$G(V)=\frac{e^2}{h}\sum_n\left[T^{(n)}_{\mathrm{ReLe}}(V)+2T^{(n)}_{\mathrm{LhLe}}(V)+T^{(n)}_{\mathrm{RhLe}}(V)\right], \tag{25}$$

where $T^{(n)}_{\mathrm{ReLe}}(V)$, $T^{(n)}_{\mathrm{LhLe}}(V)$, $T^{(n)}_{\mathrm{RhLe}}(V)$ denote normal transmission, local Andreev reflection, and crossed Andreev reflection coefficients for incident electrons from the left lead by absorbing (emission) $|n|$ photons if $n>0$ ($n<0$) and outgoing electron (or hole) to the left or right leads. It can be evaluated that Eqs. (23) and (25). is consistent with the results in Ref. [21] once returning to static limit ($A=0$). Additionally, the derivation of the current for the periodically driven single impurity is analogical, except that the R lead is replaced by the superconductor terminal S.

B. Numerical results for anomalous photon-assisted tunneling

With the help of the Floquet Green's function and iterative method (see Appendix A), we can numerically calculate the time-averaged conductances. Here we take the low-temperature limits and set $\widetilde{\Delta}=220\,\mu$eV, $\alpha_R=0.28$ eV Å and effective mass $m^*=0.02m_e$ (m_e is the mass of the electron) [10,21]. The lattice constant $a=3.5$ nm and the resulting nearest hopping energy is $t_N=\hbar^2/(2m^*a^2)\approx 156$ meV. The coupling is $\widetilde{\Gamma}^L=\widetilde{\Gamma}^R=0.05t_N$ for the 1D Majorana nanowire. For the single impurity, we set $E_0=0$ and $\widetilde{\Gamma}^{sc}=\widetilde{\Gamma}^L=0.05$ in the unit of $\hbar\omega$.

In Figs. 1(c) to 1(f), the time-averaged conductances G are shown as functions of relative field strength $A_R=\frac{A}{\hbar\omega}$ and the bias for the microwave-driven MBSs and single impurity. Figures 1(e) and 1(f) are the cutoff of Figs. 1(c) and 1(d). When the driving field is absent ($A_R=0$), both trivial ABSs and MBSs contribute a ZBCP. As A_R climbs, the height of ZBCP for the single impurity changes dramatically and PAT sideband peaks emerges obviously at harmonics $V=0,\pm1\hbar\omega,\pm2\hbar\omega,\ldots$, indicating the absorption and emission of photons [Figs. 1(d) and 1(f)]. But the ZBCP in the conductance spectroscopy remains the same and no PAT peaks appears in the case of MBSs, see Figs. 1(c) and 1(e). This means no interaction between MBSs with $Q=0$ and photons. In the case of applying the harmonic magnetic field $(0,\quad 0,\quad A\cos(\omega t))$, similar results are exhibited, see Figs. 2(a) to 2(d). PAT sideband peaks disappear for MBSs in Figs. 2(a) and 2(c), but arise for single impurity in Figs. 2(b) and 2(d). This supports our argument that ζ_z for MBS is also zero.

When the Majorana nanowire length N decreases, two MBSs located at two opposite ends will overlap and lead to an energy splitting. In the meantime the lowest-energy states ψ_0 formed by two MBSs will recover finite BCS charge Q [as Eq. (14) suggests]. In Figs. 3(a) and 3(b), we show the time-averaged conductances for different nanowire lengths when $A_R=0$ and $A_R=2$. Due to the enhanced hybridization between two MBSs, the ZBCP splits into two peaks as the nanowire becomes short. The stronger splitting is accompanied by a greater asymmetry of electron-hole components and more obvious PAT side peaks. This anomalous PAT signal is consistent with our preceding analysis. The disappearance of the PAT signal actually reflects that a MBS remains

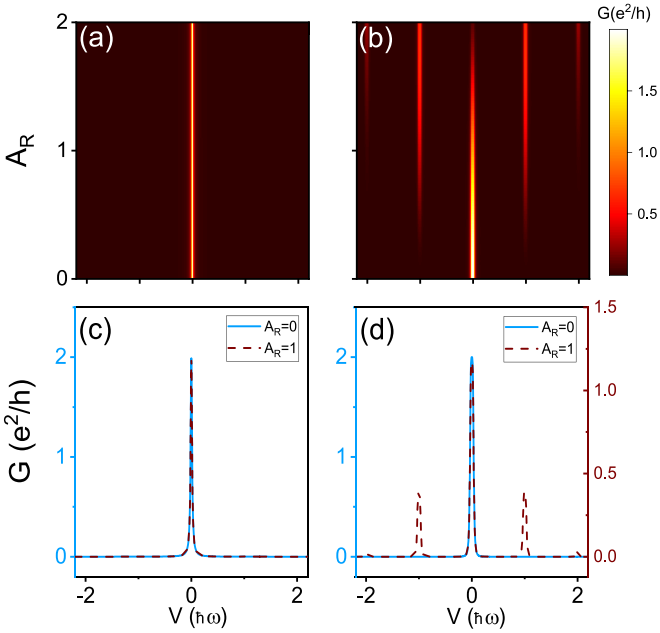

FIG. 2. (a)–(d) The time-averaged conductances for the (a,c) MBSs and (b,d) single impurity driven by the harmonic magnetic field as functions of A_R and bias V. Parameters are the same as Figs. 1(c) to 1(f).

unperturbed by local electromagnetic noise, which is crucial to implement a topological qubit.

Besides the cases for MBSs and single impurity shown in Fig. 1, the real situation may be more complicated since MBSs and near-zero energy ABSs possibly coexist in the nanowire. At this time, PAT may still emerge due to the near-zero energy ABSs, even if MBSs are well separated. MBSs' information here is inevitably interfered by ABSs. However, from the perspective of the application, the coexistence of MBSs and near-zero energy ABSs may not serve to prepare for topological qubits since the probe is hard to be assured to selectively couple to one single MBS. Although MBSs cannot be well confirmed in this case, it has little application potential. What the experiment should pay attention for applications should be the case where PAT disappears.

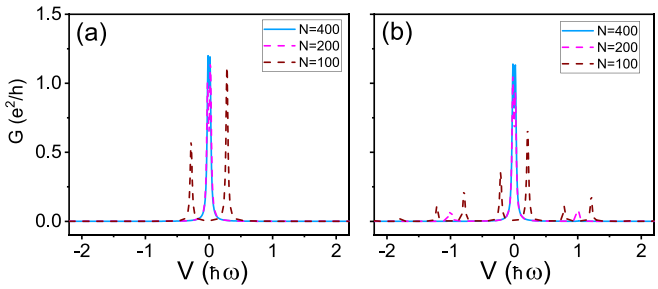

FIG. 3. Time-averaged conductances G vs. bias V for different nanowire lengths N with $A_R =$ (a) 0 and (b) 2. All the other parameters are the same as Fig. 1(e).

IV. MEASUREMENT OF BCS CHARGE

A. Analytic form of time-averaged conductance

Based on the projected Hamiltonian in Eq. (8), we are able to analyze how BCS information enters into time-averaged conductance. Take the microwave-driving field as an example, the resulting projected self-energy terms of normal leads in the lowest-energy states space are $\mathbf{\Sigma}^{r,p} = \mathbf{\Sigma}_L^{r,p} + \mathbf{\Sigma}_R^{r,p}$ with

$$\mathbf{\Sigma}^{r,p}_{\alpha=L,R} = \begin{pmatrix} -i\frac{\gamma_\alpha}{2} & -i\frac{\xi_\alpha}{2}^* \\ -i\frac{\xi_\alpha}{2} & -i\frac{\gamma_\alpha}{2} \end{pmatrix}, \tag{26}$$

where $\gamma_\alpha = \tilde{\Gamma}^\alpha n_\alpha$, $n_L = \sum_s (|u_{1s}^{(0)}|^2 + |v_{1s}^{(0)}|^2)$, $n_R = \sum_s (|u_{Ns}^{(0)}|^2 + |v_{Ns}^{(0)}|^2)$, $\xi_L = \tilde{\Gamma}^L \sum_s 2u_{1s}^{(0)} v_{1s}^{(0)}$, $\xi_R = \tilde{\Gamma}^R \sum_s 2u_{Ns}^{(0)} v_{Ns}^{(0)}$. We also introduce $\gamma_{Le} = \sum_s \tilde{\Gamma}^L |u_{1s}^{(0)}|^2$, $\gamma_{\mathrm{Re}} = \sum_s \tilde{\Gamma}^R |u_{Ns}^{(0)}|^2$, $\gamma_{Lh} = \sum_s \tilde{\Gamma}^L |v_{1s}^{(0)}|^2$, $\gamma_{Rh} = \sum_s \tilde{\Gamma}^R |v_{Ns}^{(0)}|^2$. The linewidth functions are

$$\mathbf{\Gamma}^{\alpha,p} = i\left(\mathbf{\Sigma}_\alpha^{r,p} - \mathbf{\Sigma}_\alpha^{a,p}\right) = \mathbf{\Gamma}_e^{\alpha,p} + \mathbf{\Gamma}_h^{\alpha,p} = \begin{pmatrix} \gamma_\alpha & \xi_\alpha^* \\ \xi_\alpha & \gamma_\alpha \end{pmatrix}. \tag{27}$$

Starting from Eqs. (8) and (26), we can use the Dyson equation introduced in Ref. [38] to obtain the analytic expressions for differential conductances (see details in Appendix B). Under the weak coupling strength ($\tilde{\Gamma}^\alpha \to 0$) and low-temperature limits, the $G(V)$ at the harmonics $V = \varepsilon_0 + n\hbar\omega$ ($\varepsilon_0 \neq 0, n = 0, \pm 1, \dots$) denoted as G_n can analytically be obtained as

$$G_n \approx \frac{e^2}{h} \frac{4\gamma_{Lh}}{\gamma^2} (\gamma_R + 2\gamma_{Le}) J_n^2 (QA_R), \tag{28}$$

where $\gamma = \gamma_L + \gamma_R$ and $J_n(QA_R)$ is the nth-order Bessel function of argument QA_R. Close to $V = -\varepsilon_0 + n\hbar\omega$, the conductances are the same as Eq. (28) except for exchanging e and h. Equation (28) clearly suggest that the height of PAT peaks are relevant to the BCS charge of the subgap bound state. It indicates that we can extract the BCS charge from the ratio of peak heights

$$G_1/G_0 = J_1^2 (QA_R)/J_0^2 (QA_R). \tag{29}$$

It is worth mentioning that here we use a local conductance to detect the BCS charge. Compared with nonlocal conductances, local conductance will give a stronger signal [21].

B. BCS charge extraction from the conductance spectroscopy

We try to numerically explore the time-averaged conductance as a function of chemical potential μ (see Fig. 4) and Zeeman field V_0 (see Fig. 5) for the microwave-driven Majorana nanowire. In Fig. 4, without the driving field ($A_R = 0$), the energy-gap closure occurs at $\mu = \mu_c \approx \pm 550\,\mu$eV, which is roughly the topological transition point $\mu_c = \pm\sqrt{V_0^2 - \widetilde{\Delta}^2}$ [8,9]. The ZBCP appears, and the nanowire is in the topological phase with a pair of MBSs when $|\mu| < \mu_c$. With the increase of μ from $-\mu_c$, the ZBCP is almost unaffected at low μ, but gradually split and the lowest-energy states ε_0 present the characteristics of typical Majorana oscillation [see Figs. 4(a) and 4(c)] [50]. The enhancement of the split (i.e., ε_0) originates from the increase of the coupling strength between MBSs when μ raises. After applying the

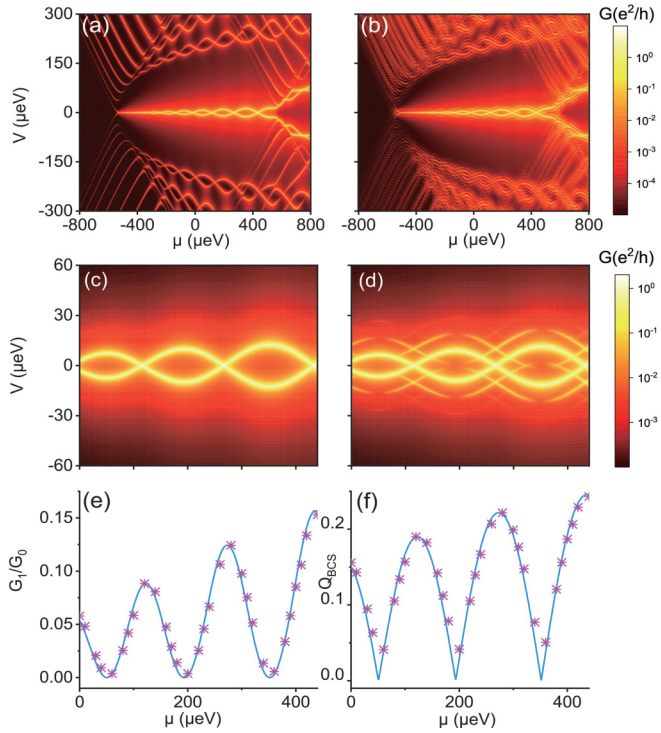

FIG. 4. (a)–(d) Time-averaged conductances G of microwave-driven Majorana nanowire as functions of μ and bias V with $A_R =$ (a, c) 0 and (b, d) 3. (c, d) are the enlarged views of the low energy part in (a, b). (e) The comparison between extracted G_1/G_0 (pink stars) from (d) and $J_1^2(QA_R)/J_0^2(QA_R)$ (blue line) with Q obtained from H_{nw} diagonalization. (f) The comparison between $Q_{\rm BCS}$ from conductance ratios G_1/G_0 (pink stars) and "actual" $Q_{\rm BCS}$ from direct diagonalization of H_{nw} (blue line). The parameters $N = 400$, $V_0 = 600\,\mu$eV, and $\hbar\omega = 10\,\mu$eV.

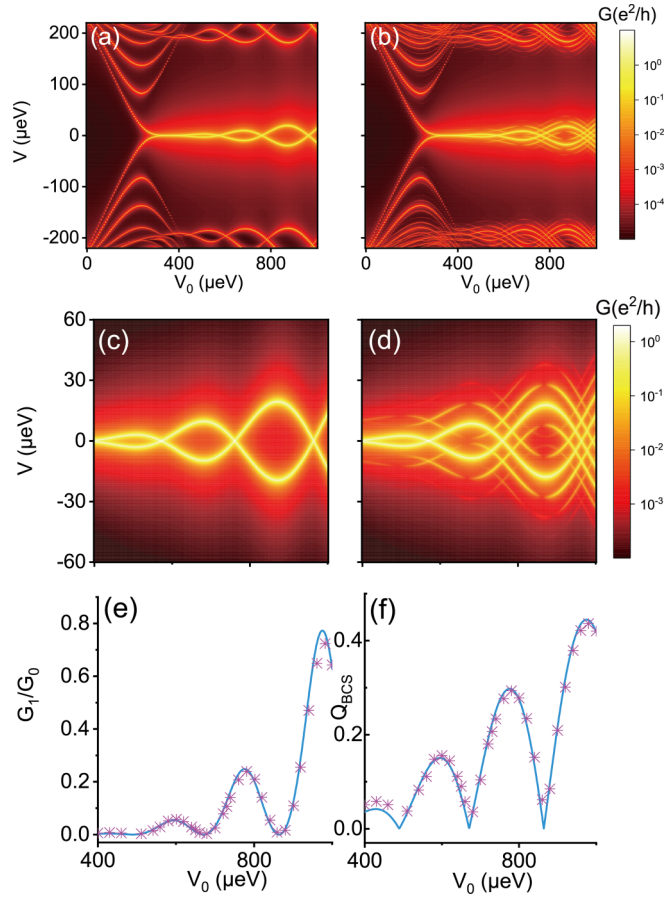

FIG. 5. (a)–(d) Time-averaged conductances G of microwave-driven Majorana nanowire as functions of static Zeeman field V_0 and bias V at $\mu = 0$ when (a, c) $A_R = 0$ and (b, d) $A_R = 3$. (c) and (d) are the enlarged views of (a) and (b). (e) The comparison between G_1/G_0 (pink stars) extracted from (d) and $J_1^2(QA_R)/J_0^2(QA_R)$ (blue line) where Q is just BCS charge obtained from Hamiltonian H_{nw} diagonalization. (f) The comparison between $Q_{\rm BCS}$ obtained from conductances ratios G_1/G_0 (pink stars) and "actual" $Q_{\rm BCS}$ from direct diagonalizing H_{nw}. The other parameters are the same as Fig. 4.

microwave field ($A_R = 3$), the conductance spectroscopy becomes complicated [Fig. 4(b)]. Massive PAT sideband peaks concentrate on the region beyond the induced topological gap where electron-like and hole-like quasiparticle states stay. Near ZBCP, the photonic sideband peaks appear to be more obvious as μ grows. From the enlarged view only concerning of the lowest-energy state in Fig. 4(d), these sideband peaks can be seen clearly, as a result of the coupling of MBSs leading to a nonzero BCS charge Q. In Fig. 4(e), we can extract a series of conductance peak ratios G_1/G_0 of zeroth and first harmonics from Fig. 4(d), and also show $J_1^2(QA_R)/J_0^2(QA_R)$ with Q obtained by numerically diagonalizing the isolated nanowire Hamiltonian H_{nw}. There is a strong correlation between G_1/G_0 (pink stars) and $J_1^2(QA_R)/J_0^2(QA_R)$ (blue line). Furthermore, in Fig. 4(f), we use these extracted conductance ratios G_1/G_0 to fit Eq. (29) to obtain $Q_{\rm BCS}$ (pink stars). It is found to be well consistent with the "actual" $Q_{\rm BCS}$ (blue line) from H_{nm} diagonalization [51]. Comparing Figs. 4(d) and 4(f), the BCS charge and energy splitting oscillate out of phase due to Q is equal to $\frac{d\varepsilon_0}{d\mu}$ [21].

Similar results are shown by varying the static Zeeman field V_0 in Fig. 5. With $A_R = 0$, a gap closure and ZBCP appears at $V_0 \approx 300\,\mu$eV because of the topological transition in Fig. 5(a). Then, as V_0 grows, a Majorana oscillation can be also observed as the Zeeman field also modulates MBSs' coupling strength [see Figs. 5(a) and 5(c)]. When the microwave field exists ($A_R = 3$), PAT sideband peaks emerge clearly in Figs. 5(b) and 5(d). We can repeat the previous process to compare G_1/G_0 and extract the BCS charge. The results still match the expectations [see Figs. 5(e) and 5(f).] In general, this provides a reliable way to detect BCS charges by measuring the conductance ratios G_1/G_0. In principle, if the driving field is locally applied on the wire, the local BCS charge information can be also extracted.

V. MEASUREMENT OF BCS SPIN COMPONENTS

Enlightened by the Eq. (8), we consider that the Majorana nanowire is driven by both the harmonic magnetic field along the z direction and the microwave field. The external field

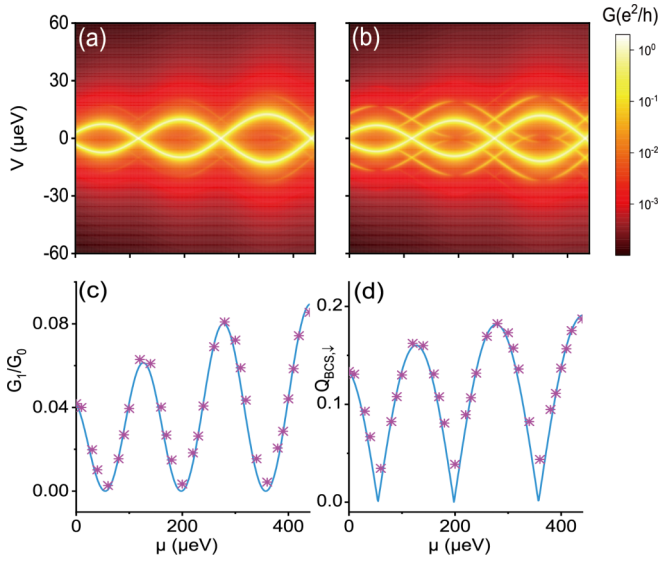

FIG. 6. (a, b) Time-averaged conductance G versus μ and V at $V_0 = 600\,\mu$eV under the joint external field H_{f1}. The initial phases of the two fields are (a) $\phi_1 = \phi_2 = 0$ and (b) $\phi_1 = 0, \phi_2 = \pi$. (c) The comparison between the extracted G_1/G_0 (pink stars) from (b) and $J_1^2(Q_\downarrow A_R)/J_0^2(Q_\downarrow A_R)$ (blue line). (d) The $Q_{\mathrm{BCS},\downarrow}$ obtained from the G_1/G_0 in (b) (pink stars) and "actual" $Q_{\mathrm{BCS},\downarrow}$ by diagonalizing Hamiltonian H_{nm} (blue line). Other parameters are the same as Fig. 4.

Hamiltonian is

$$\begin{aligned} H_{f1} &= H_{fm} + H_{fz} \\ &= \sum_{i,s} \frac{A}{2} \cos(\omega t + \phi_1)\, c_{is}^\dagger c_{is} \\ &\quad + \sum_{i,s,s'} \frac{A}{2} \cos(\omega t + \phi_2)\, c_{is}^\dagger (\sigma^z)_{ss'} c_{is'}. \end{aligned} \tag{30}$$

Here we set the amplitude of two fields as equal, which can be realized even without knowing the g-factor (see Appendix C). When the two fields have the same initial phase $\phi_1 = \phi_2 = 0$, the renormalization factor in Eq. (8) is $Q_\uparrow = \sum_i(|u_{i\uparrow}^{(0)}|^2 - |v_{i\uparrow}^{(0)}|^2)$. But the renormalization factor is $Q_\downarrow = \sum_i(|u_{i\downarrow}^{(0)}|^2 - |v_{i\downarrow}^{(0)}|^2)$ when two initial phases have π difference (e.g., $\phi_2 = \pi, \phi_1 = 0$). So we expect that $Q_\uparrow$ and $Q_\downarrow$, the BCS spin components along the z direction, can be measured from conductance ratios under this joint field.

Figure 6 shows time-averaged G as a function of μ under the joint field with $\phi_1 = \phi_2 = 0$ [Fig. 6(a)] and $\phi_1 = 0, \phi_2 = \pi$ [Fig. 6(b)], respectively. Here the PAT peaks also exhibit as expected. Moreover, they are much clearer in Fig. 6(b) than in Fig. 6(a). The reason is that the BCS charge for overlapping MBSs has a spin polarization : $Q_{\mathrm{BCS},\downarrow} \gg Q_{\mathrm{BCS},\uparrow}$. This conforms to the fact that the Majorana wave function has large spin $\downarrow$ component for a strong magnetic field. From Fig. 6(b), we directly extract G_1/G_0 (pink stars) and find it is well consistent with $J_1^2(Q_\downarrow A_R)/J_0^2(Q_\downarrow A_R)$ (blue line) see Fig. 6(c). Similarly, in Fig. 6(d), $Q_{\mathrm{BCS},\downarrow}$ can be obtained by fitting Eq. (29) using the extracted G_1/G_0 (pink stars), and is almost the same as the "actual" $Q_{\mathrm{BCS},\downarrow}$ (blue line) by diagonalizing

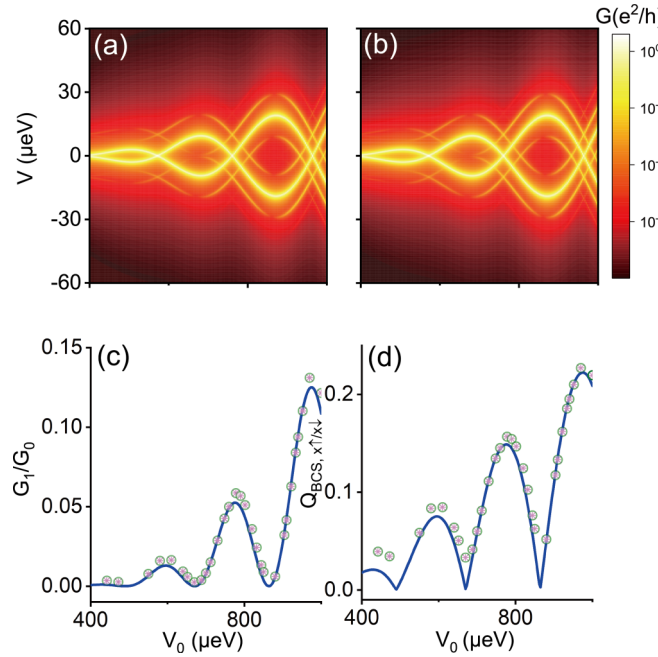

FIG. 7. (a, b) Time-averaged conductance G versus V_0 and V at $\mu = 0$ under the joint external field H_{f2}. The initial phases of the two fields are (a) $\phi_1 = \phi_2 = 0$ and (b) $\phi_1 = 0, \phi_2 = \pi$. (c) The comparison between the extracted G_1/G_0 [pink stars for (a) and green circles for (b)] and $J_1^2(QA_R)/J_0^2(QA_R)$ where $Q = \sum_i(|u_{i,x\uparrow/x\downarrow}^{(0)}|^2 - |v_{i,x\uparrow/x\downarrow}^{(0)}|^2)$ (both of the spin components are represented by dark blue lines due to the coincidence). (d) The Q_{BCS} obtained from the G_1/G_0 [pink stars for (a) and green circles for (b)] and "actual" Q_{BCS} by diagonalizing Hamiltonian H_{nm} (dark blue line for both spin components). Other parameters are the same as Fig. 4.

Hamiltonian H_{nw} (due to errors in the numerical extraction process, the deviations may occur when $Q_{\mathrm{BCS}} \to 0$).

The BCS spin component along any direction can be obtained by choosing an appropriate harmonic magnetic field direction, in principle. For example, when the Majorana nanowire is driven by both a harmonic magnetic field along the x direction and the microwave field. The external field Hamiltonian is

$$\begin{aligned} H_{f2} &= H_{fm} + H_{fx} \\ &= \sum_{i,s} \frac{A}{2} \cos(\omega t + \phi_1)\, c_{is}^\dagger c_{is} \\ &\quad + \sum_{i,s,s'} \frac{A}{2} \cos(\omega t + \phi_2)\, c_{is}^\dagger (\sigma^x)_{ss'} c_{is'}. \end{aligned} \tag{31}$$

Similarly, we can extract the BCS spin component $Q_{x\uparrow,x\downarrow}$ along the x direction by adjusting phases $\phi_1 = \phi_2 = 0$ or $\phi_1 = 0, \phi_2 = \pi$, as shown in Figs. 7(a) to 7(d). Different from Fig. 6, the conductance spectroscopies for $\phi_1 = \phi_2 = 0$ in Fig. 7(a) and $\phi_1 = 0, \phi_2 = \pi$ in Fig. 7(b) are totally the same, as a result of $Q_{\mathrm{BCS},x\uparrow} = Q_{\mathrm{BCS},x\downarrow}$. This equality origins from the symmetry of our model. It also means BCS spin polarization along the x direction $\zeta_x = \sum_{i,s}(u_{is}u_{i\bar{s}}^* - v_{is}v_{i\bar{s}}^*)$ is zero [52] ($\bar{s}$ is the opposite direction of spin s). Besides, we also compare the conductance ratios G_1/G_0 and $Q_{\mathrm{BCS},x\uparrow,x\downarrow}$

with $J_1^2(QA_R)/J_0^2(QA_R)$ and the "actual" $Q_{\mathrm{BCS},x\uparrow,x\downarrow}$ from the H_{nm} diagonalization. As shown in Figs. 7(c) and 7(d), the comparison results are still consistent.

VI. SUMMARY AND DISCUSSION.

In this paper, we show an anomalous PAT for the MBS where the sideband peaks are correlated with Majorana nonlocality in the periodically driven Majorana nanowire. The PAT sideband peaks should disappear for well-separated MBSs, but reappear for overlapping MBSs. We also investigate the conductance spectroscopy by varying chemical potential and Zeeman field to study the PAT characteristics for Majorana oscillations. In addition, a systematic scheme is further proposed to measure the BCS information of subgap states.

For the experiment realizations, PAT in the periodically driven Majorana nanowire is, in principle, attainable, especially in view that the research for PAT and the periodically driven system has developed as a mature field and covered a wide range as stated in the Introduction. For instance, the interplay between the microwave driving field and superconductors, which has produced many works in recent years such as the measurement of the 4π periodic Josephson effect [53] and PAT into YSR states [54]. One experiment very related to our setup is a recent work considering two coupled Majorana nanowires where one of them is applied by microwave field [55]. They investigate the PAT signals on the charge stability diagram and give a spectroscopic measurement of interpair coupling E_M between zero modes on two superconducting islands. Our device is similar to them for one periodically driven Majorana nanowire coupled to two normal leads and should be also achievable.

One potential question of our scheme in the experiment detection may be that thermal broadening could cover the sideband peaks. Then, the PAT signals in our previous results may be all invisible. The thermal broadening from the finite-temperature effect ignored in our calculation can be calculated as a convolution with the derivative of the Fermi distribution. It will affect the line shape of conductance peaks in the same way, thus does not affect the conductances peaks' ratios [21]. In the experiment, the temperature T is usually tens of mK corresponding to several μeV for thermal broadening k_BT (k_B is the Boltzmann constant). This is much lower than the superconducting gap, which is a few hundreds of μeV [10]. Therefore, by adjusting the experiment's parameters appropriately, the case satisfying (Γ, k_BT) (peaks broadening, several μeV) $\ll \hbar\omega$ (photon energy, $\sim 10\,\mu$eV) $\ll \widetilde{\Delta}$ (superconducting gap, several $100\,\mu$eV) is possible, in principle, to be realized to make the sideband peaks distinct.

Although Majorana fermions are proved to exhibit an anomalous PAT in our work, it still remains a question whether this can be used to identify the emergence of topological MBSs in the experiment, especially considering the various complex situations in the present experiments. This is, of course, not the main goal of our work. Here we could conclude some remarks. Overall, anomalous PAT sideband peaks have a connection with the Majorana nonlocality or BCS charge of subgap states. According to Ref. [56], the origin of ZBCP can be divided into three scenarios: good, bad, and ugly. Only subgap states for the good ZBCP case corresponds to a pair of topological MBSs (i.e., two MBSs located at two ends of the nanowire). For the bad or ugly cases, the near-zero energy ABSs are composed of two partially or highly overlapped MBSs. Therefore, from their differences on Majorana nonlocality, PAT sideband peaks or BCS charge should exhibit distinguishable characteristics for good and bad/ugly cases within a range of parameters, in principle. But some special cases, such as partially separated ABSs composed of two MBSs separated by a distance of order of Majorana decay length [57,58] or quasi-Majoranas with two opposite spin polarizations [43], may still need more detailed information. Additionally, the BCS spin information, which can be extracted in our scheme, is also helpful. For example, when quasi-MBSs and overlapping MBSs have a finite BCS charge, given their difference on spin polarizations, it is expected to extract BCS spin information and find $Q_{\mathrm{BCS},\downarrow} \gg Q_{\mathrm{BCS},\uparrow}$ for topological MBSs (see Fig. 6) and $Q_{\mathrm{BCS},\downarrow} \approx Q_{\mathrm{BCS},\uparrow}$ for quasi-MBSs. In short, our scheme is at least able to provide some prejudgments for the existence of topological MBSs or for topological qubit implementation, in view of the close link between BCS charge and Majorana nonlocality.

ACKNOWLEDGMENTS

This work was financially supported by National Key R and D program of China (Grant No. 2017YFA0303301), NSF-China (Grant No. 11921005) and the Strategic Priority Research Program of Chinese Academy of Sciences (Grant No. XDB28000000).

APPENDIX A: FLOQUET GREEN'S FUNCTIONS IN FLOQUET EXTENDED SPACE

In this Appendix, we briefly introduce how to compute those Floquet Green's functions in Sec. III. For a more expansive and detailed description, see Refs. [35,36,45]. We first write the time-dependent Shrödinger equation (in units of $\hbar = 1$)

$$i\partial_t \psi_j(t) = H(t)\,\psi_j(t), \tag{A1}$$

where $H(t+T) = H(t)$ under the periodically driving field. The wave function $\psi_j(t)$ can be decomposed into $\psi_j(t) = \sum_m e^{-i\epsilon_j t + im\omega t}\widetilde{\psi}_j^m$ in the Floquet extended space. Substituting this expression into Eq. (A1) and multiplying on the left by $\frac{1}{T}\int_0^T dt e^{-in\omega t}$, we can get

$$H^F\widetilde{\psi}_j = \epsilon_j\widetilde{\psi}_j, \tag{A2}$$

where $\widetilde{\psi}_j$ is a vector in the Floquet extended space, H^F is the Floquet Hamiltonian, and its components can be defined as

$$\begin{aligned} H^F_{nm} &= \frac{1}{T}\int_0^T dt e^{-in\omega t}\left(H(t) - i\partial_t\right)e^{im\omega t} \\ &= \frac{1}{T}\int_0^T dt e^{i(m-n)\omega t}H(t) + m\omega\delta_{nm}. \end{aligned} \tag{A3}$$

Thus the time-dependent Hamiltonian in Eq. (A1) will be just changed into the time-independent Hamiltonian in Eq. (A2), by considering the m and n index as the Floquet basis. Similarly, we can give the retarded Floquet Green's function with

the help of the Dyson equation in the Floquet extended space

$$G^{r,-1}(E) = E * I - H^F - \sum_{\alpha=L,R} \Sigma^r_\alpha, \tag{A4}$$

where I is the identity matrix. The Floquet Hamiltonian for our system is

$$\mathbf{H}^F = \begin{pmatrix} \cdots & \mathbf{H}_1 & \mathbf{0} & \mathbf{0} & \cdots \\ \cdots & \mathbf{H}_0 - \omega \mathbf{I}_{4N\times 4N} & \mathbf{H}_1 & \mathbf{0} & \cdots \\ \cdots & \mathbf{H}_{-1} & \mathbf{H}_0 & \mathbf{H}_1 & \cdots \\ \cdots & \mathbf{0} & \mathbf{H}_{-1} & \mathbf{H}_0 + \omega \mathbf{I}_{4N\times 4N} & \cdots \\ \cdots & \mathbf{0} & \mathbf{0} & \mathbf{H}_{-1} & \cdots \end{pmatrix}, \tag{A5}$$

where N is the number of lattice sites for the nanowire. H_0 is just the nanowire Hamiltonian H_{nm}. The off-diagonal elements $H_{1,-1}$ is related to the periodically driving field: $\mathbf{H}_1 = (\mathbf{H}_{-1})^\dagger = \frac{A}{2}\tau^z I_{2N\times 2N}$ for the microwave field and $\frac{A}{2}\sigma^z\tau^z I_{N\times N}$ for the harmonic magnetic field along the z direction. The Σ^r_α is the self-energy from normal leads α and is related to the linewidth function matrix

$$\begin{aligned} \mathbf{\Gamma}^{L,R} &= i\left(\mathbf{\Sigma}^r_{L,R} - \mathbf{\Sigma}^a_{L,R}\right)_{4NM\times 4NM} \\ &= \begin{pmatrix} \left(\mathbf{\Gamma}^{L,R}_e\right)_{2NM\times 2NM} & 0 \\ 0 & \left(\mathbf{\Gamma}^{L,R}_h\right)_{2NM\times 2NM} \end{pmatrix}, \end{aligned} \tag{A6}$$

with M is the Floquet space dimension, which is infinite in principle. $\Sigma^r = (\Sigma^a)^\dagger$. $(\mathbf{\Gamma}^L_{e,h})_{ij,lr;mn} = \widetilde{\Gamma}^L \delta_{ij}\delta_{i1}\delta_{lr}\delta_{mn}$ and $(\mathbf{\Gamma}^R_{e,h})_{ij,lr;mn} = \widetilde{\Gamma}^R \delta_{ij}\delta_{iN}\delta_{lr}\delta_{mn}$, where l, r only take the value of 1,2 for the electron part and 3,4 for the hole part. To conduct numerical calculations in our main text, we truncate the Floquet space dimension into $[-7, 7]$ ($M = 15$). In addition, with the help of recursive Green's function equations

$$\begin{aligned} G^{(i+1),r}_{i+1,i+1}(E) &= \left[g^{(0),-1}_{i+1,i+1}(E) - V_{i+1,i} G^{(i),r}_{i,i}(E) V_{i,i+1}\right]^{-1}, \\ G^{(i+1),r}_{1,i+1}(E) &= G^{(i),r}_{1,i}(E) V_{i,i+1} G^{(i+1),r}_{i+1,i+1}(E), \end{aligned} \tag{A7}$$

where G^r is the dressed Green's function involving the couplings between the sites, $g^{(0)}$ is the isolated Green's function for one site, $V_{i,j}$ is the hopping energy between site i and site j, we can obtain the $G^r_{n,n}$ and $G^r_{1,n}$ for any n starting from $G^{(1),r}_{1,1} = g^{(0)}_{1,1}$. We also denote all these terms on the sites are put in the Floquet $\bigotimes$ BdG space.

APPENDIX B: DERIVATIONS OF ANALYTIC FORM FOR THE TIME-AVERAGED CONDUCTANCES

In this Appendix, we try to analyze the Floquet Green's functions in the projected space $(\psi_0^\dagger, \psi_0)$. Using the Dyson equation, we can express the retarded Green's function $G^{r,p}$ in the projected space as [38]

$$\begin{aligned} G^{r,p}_{11;mn} &= g^{r,p}_{11;mn} + \sum_{n_1,n_2} G^{r,p}_{11;mn_1}\left(\Sigma^{r,p}_{11;n_1n_1}\delta_{n_1,n_2} + \Sigma^{r,p}_{12;n_1n_1} D_{22;n_1n_2} \Sigma^{r,p}_{21;n_2n_2}\right) g^{r,p}_{11;n_2n}, \\ G^{r,p}_{22;mn} &= g^{r,p}_{22;mn} + \sum_{n_1,n_2} G^{r,p}_{22;mn_1}\left(\Sigma^{r,p}_{22;n_1n_1}\delta_{n_1,n_2} + \Sigma^{r,p}_{21;n_1n_1} D_{11;n_1n_2} \Sigma^{r,p}_{12;n_2n_2}\right) g^{r,p}_{22;n_2n}, \\ G^{r,p}_{12;mn} &= \sum_{n_1} G^{r,p}_{11;mn_1} \Sigma^r_{12;n_1n_1} D_{22;n_1n}, \\ G^{r,p}_{21;mn} &= \sum_{n_1} G^{r,p}_{22;mn_1} \Sigma^{r,p}_{21;n_1n_1} D_{11;n_1n}, \end{aligned} \tag{B1}$$

where $\Sigma^{r,p}_{mn} = \Sigma^{r,p}\delta_{nm}$ due to the time independence and $\Sigma^{r,p}$ corresponds exactly to Eq. (26). Here the first two indices denote the Nambu spinor in the projected space $(\psi_0^\dagger, \psi_0)$ and the other two indices denote Fourier indices or Floquet indices. Based on Eq. (8), the bare Green's function $g^{r,p}_{mn}$ without coupling to normal leads is derived as (in units of $\hbar = 1$)

$$g^{r,p}_{mn} = \begin{pmatrix} \sum_k \frac{J_{k+m}(QA_R)J_{k+n}(QA_R)}{\varepsilon - \varepsilon_0 - k\omega + i0^+} & 0 \\ 0 & \sum_k \frac{J_{k-m}(QA_R)J_{k-n}(QA_R)}{\varepsilon + \varepsilon_0 + k\omega + i0^+} \end{pmatrix}. \tag{B2}$$

Here $A_R = A/\omega$. In addition, $D_{ii;mn}$ $(i = 1, 2)$ in Eq. (B1) can be calculated using the recursive method

$$D_{ii;mn} = g^{r,p}_{ii;mn} + \sum_{m_1} g^{r,p}_{ii;mm_1} \Sigma^{r,p}_{ii;m_1m_1} g^{r,p}_{ii;m_1n} + \cdots. \tag{B3}$$

In the approximation of $\omega \gg \gamma = \gamma_L + \gamma_R$ ($\gamma_{L,R}$ is defined in Sec. IV), we can take the approximation [38]

$$\sum_{n,m} \frac{f_{nm}}{(\varepsilon + \varepsilon_0 + n\omega + i0^+)(\varepsilon + \varepsilon_0 + m\omega + i0^+)} \approx \sum_n \frac{f_{nn}}{(\varepsilon + \varepsilon_0 + n\omega + i0^+)^2} \tag{B4}$$

for any function f_{nm}. Thus, the projected retarded Green's functions of Eq. (B1) can be summarized as

$$G^{r,p}_{11;mn} = \sum_k \frac{J_{m+k}(QA_R)\,J_{n+k}(QA_R)}{\varepsilon-\varepsilon_0-k\omega+i\frac{\gamma}{2}+\sum_l \frac{J^2_{k+l}(2QA_R)|\xi|^2/4}{\varepsilon+\varepsilon_0+l\omega+i\frac{\gamma}{2}}},$$

$$G^{r,p}_{22;mn} = \sum_k \frac{J_{k-m}(QA_R)\,J_{k-n}(QA_R)}{\varepsilon+\varepsilon_0+k\omega+i\frac{\gamma}{2}+\sum_l \frac{J^2_{k+l}(2QA_R)|\xi|^2/4}{\varepsilon-\varepsilon_0-l\omega+i\frac{\gamma}{2}}},$$

$$G^{r,p}_{12;mn} = \sum_{ks} \frac{J_{m+k}(QA_R)\,J_{s-n}(QA_R)\,J_{k+s}(2QA_R)}{\left(\varepsilon-\varepsilon_0-k\omega+i\frac{\gamma}{2}+\sum_l \frac{J^2_{k+l}(2QA_R)|\xi|^2/4}{\varepsilon+\varepsilon_0+l\omega+i\frac{\gamma}{2}}\right)\left(\varepsilon+\varepsilon_0+s\omega+i\frac{\gamma}{2}\right)}(-i\xi^*/2),$$

$$G^{r,p}_{21;mn} = \sum_{ks} \frac{J_{k-m}(QA_R)\,J_{s+n}(QA_R)\,J_{k+s}(2QA_R)}{\left(\varepsilon+\varepsilon_0+k\omega+i\frac{\gamma}{2}+\sum_l \frac{J^2_{k+l}(2QA_R)|\xi|^2/4}{\varepsilon-\varepsilon_0-l\omega+i\frac{\gamma}{2}}\right)\left(\varepsilon-\varepsilon_0-s\omega+i\frac{\gamma}{2}\right)}(-i\xi/2). \tag{B5}$$

Here $\xi = \xi_L + \xi_R$ where $\xi_{L,R}$ is defined in Sec. IV. Now we focus on the region close to harmonics, namely near $\varepsilon = \pm\varepsilon_0 + n\omega$ ($\varepsilon_0 > 0, n = \cdots -1, 0, 1, 2\cdots$). For convenience, we denote the time-averaged conductances at these resonant levels as G_n. Despite the lattice indices no longer existing due to projection operation on the lowest-energy states, we can still substitute Green's functions in Eq. (B5) along with linewidth functions in Eq. (27) into Eqs. (24) and (25) to obtain transmission coefficients and the resulting conductance (all of these quantities are regarded as matrices in the projected space with Floquet indices). Considering the weak coupling limit ($\gamma_L + \gamma_R \ll \omega$), the time-averaged differential conductance is simplified into

$$G(V) \approx \frac{e^2}{h}\sum_k \left[(\gamma_R+2\gamma_{Le})\,\gamma_{Lh}\frac{J_k^2(QA_R)}{(V-\varepsilon_0-k\omega)^2+\frac{1}{4}\gamma^2} + (\gamma_R+2\gamma_{Lh})\,\gamma_{Le}\frac{J_k^2(QA_R)}{(V+\varepsilon_0+k\omega)^2+\frac{1}{4}\gamma^2}\right]. \tag{B6}$$

When two MBSs are well separated, $\gamma_{Lh} = \gamma_{Le} = \frac{1}{2}\gamma_L$, $\varepsilon_0 \to 0$. Also at $V = n\omega$,

$$G_n \approx \frac{4e^2}{h}\frac{\gamma_L}{\gamma}J_n^2(QA_R). \tag{B7}$$

If no driving field exists $A_R = 0$, then $n = 0$, we recover the result of quantized ZBCP $\frac{2e^2}{h}$ once $\gamma_L = \gamma_R$. When two MBSs are coupled, namely, $\varepsilon_0 > 0$, we can obtain the time-averaged conductance at $V = \varepsilon_0 + n\omega$ is

$$G_n \approx \frac{e^2}{h}\frac{4\gamma_{Lh}}{\gamma^2}(\gamma_R+2\gamma_{Le})\,J_n^2(QA_R). \tag{B8}$$

Similarly we find that at $V = -\varepsilon_0 + n\omega$, the time-averaged conductance is

$$G_n \approx \frac{e^2}{h}\frac{4\gamma_{Le}}{\gamma^2}(\gamma_R+2\gamma_{Lh})\,J_n^2(QA_R). \tag{B9}$$

Here we could find the time-averaged differential conductance peaks at harmonics are directly proportional to $J_n^2(QA_R)$.

APPENDIX C: DETERMINATION OF THE POSITION THAT TWO FIELDS MEET FOR MBS

In experiment, the g-factor of the hybrid nanowires may be modified and sometimes difficult to be determined. Aimed to MBSs, due to their wave-functions' spin polarization properties, we can still find a way to approximately locate the position that two fields are equal, even if without knowing the g-factor. By this we can move forward to obtain the g-factor and then the BCS spin components.

In Fig. 8 we focus on a pair of MBSs with finite coupling in a short nanowire, driven by the joint field

$$H_f = H_{fm} + H_{fz} = \sum_{i,ss'}\left(\frac{A}{2}(\sigma^0)_{ss'} + \frac{V_z}{2}(\sigma^z)_{ss'}\right)\cos(\omega t)c^\dagger_{is}c_{is'}. \tag{C1}$$

The amplitude of the Zeeman field is set as $V_z = 2\hbar\omega$. We increase the amplitude of microwave field A from zero. Figure 8 shows the time-averaged conductance spectroscopy for coupled MBSs. There are two high main peaks at $V = \pm\varepsilon_0$ due to the coupling of two MBSs. The PAT sideband peaks emerge at harmonics $V = \pm\varepsilon_0 \pm \hbar\omega$. With the increase of A from zero,

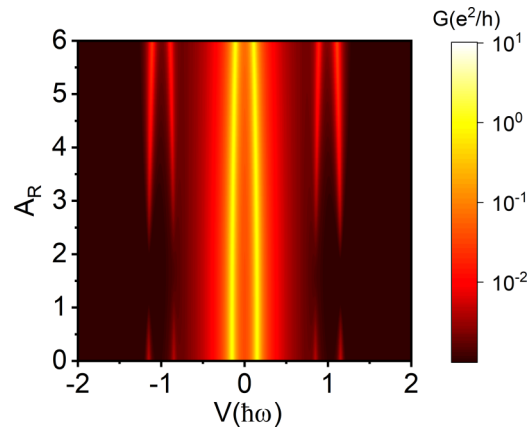

FIG. 8. The time-averaged conductance spectroscopy for weakly coupled MBSs under the joint field versus bias V and relative microwave intensity $A_R = A/\hbar\omega$. Here $\hbar\omega = 20\,\mu$eV, $V_0 = 600\,\mu$eV, and $\mu = 0$. The other parameters are the same as Fig. 4.

the PAT sideband peaks show obviously a minimum region. The minimum value of the PAT sideband peaks locate about at $A = V_z$. So from the PAT conductance spectroscopy, we can ascertain the position of $A = V_z = \frac{1}{2}g\mu_B B$ and further obtain the g-factor. The reasons are as follows: the joint driving field H_f projected to the lowest-energy states space $(\psi_0^\dagger, \psi_0)$ will be

$$\begin{aligned} H_f^p &= H_{fm}^p + H_{fz}^p \\ &= \left[\frac{A(Q_\uparrow + Q_\downarrow)}{2} + \frac{V_z(Q_\uparrow - Q_\downarrow)}{2}\right]\cos(\omega t) \\ &= \left[\frac{(A+V_z)Q_\uparrow}{2} + \frac{(A-V_z)Q_\downarrow}{2}\right]\cos(\omega t). \end{aligned} \tag{C2}$$

Here H_f^p is the effective driving field for the lowest sub-gap states. In addition, $[\frac{(A+V_z)Q_\uparrow}{2\hbar\omega} + \frac{(A-V_z)Q_\downarrow}{2\hbar\omega}]$ will also be the argument of the Bessel function, as Eq. (28) in the main text indicates. For MBSs, $|Q_\uparrow|$ is rather tinier than $|Q_\downarrow|$. As a result, the effective driving field approximately is $\frac{(A-V_z)Q_\downarrow}{2}\cos(\omega t)$. In Fig. 8, when the microwave field strength A is zero, BCS spin components $-V_z Q_\downarrow$ contribute to the external driving field. When $A < V_z$, as A grows, $|(A - V_z)Q_\downarrow|$ decreases, and the height of PAT sideband peaks also decline. At $A = V_z$, $(A - V_z)Q_\downarrow = 0$, leading to a very weak PAT sideband peak. Once A goes across V_z, $|(A - V_z)Q_\downarrow|$ increases from 0 once more and PAT sideband peaks could go up again. So PAT sideband peaks will reach around a minimum when $A = V_z$ for MBSs. In summary, in the topological MBSs system, by scanning the intensity of the microwave field to find the position for the PAT sideband peaks' minimum, we can approximately determine the point where two fields meet and further extract both of the BCS spin components. Moreover, this method could also help to estimate the g-factor.

[1] F. Wilczek, Nat. Phys. **5**, 614 (2009).
[2] A. Y. Kitaev, Phys. Usp. **44**, 131 (2001).
[3] J. Alicea, Rep. Prog. Phys. **75**, 076501 (2012).
[4] S. R. Elliott and M. Franz, Rev. Mod. Phys. **87**, 137 (2015).
[5] A. Kitaev, Ann. Phys. (NY) **303**, 2 (2003).
[6] C. Nayak, S. H. Simon, A. Stern, M. Freedman, and S. Das Sarma, Rev. Mod. Phys. **80**, 1083 (2008).
[7] D. Aasen, M. Hell, R. V. Mishmash, A. Higginbotham, J. Danon, M. Leijnse, T. S. Jespersen, J. A. Folk, C. M. Marcus, K. Flensberg, and J. Alicea, Phys. Rev. X **6**, 031016 (2016).
[8] R. M. Lutchyn, J. D. Sau, and S. Das Sarma, Phys. Rev. Lett. **105**, 077001 (2010).
[9] Y. Oreg, G. Refael, and F. von Oppen, Phys. Rev. Lett. **105**, 177002 (2010).
[10] V. Mourik, K. Zuo, S. M. Frolov, S. R. Plissard, E. P. A. M. Bakkers, and L. P. Kouwenhoven, Science **336**, 1003 (2012).
[11] K. T. Law, P. A. Lee, and T. K. Ng, Phys. Rev. Lett. **103**, 237001 (2009).
[12] L. Fu and C. L. Kane, Phys. Rev. B **79**, 161408(R) (2009).
[13] J. J. He, T. K. Ng, P. A. Lee, and K. T. Law, Phys. Rev. Lett. **112**, 037001 (2014).
[14] R. Pawlak, S. Hoffman, J. Klinovaja, D. Loss, and E. Meyer, Prog. Part. Nucl. Phys. **107**, 1 (2019).
[15] C.-H. Lin, J. D. Sau, and S. Das Sarma, Phys. Rev. B **86**, 224511 (2012).
[16] G. Ben-Shach, A. Haim, I. Appelbaum, Y. Oreg, A. Yacoby, and B. I. Halperin, Phys. Rev. B **91**, 045403 (2015).
[17] F. Domínguez, J. Cayao, P. San-Jose, R. Aguado, A. L. Yeyati, and E. Prada, npj Quantum Mater **2**, 13 (2017).
[18] E. Prada, R. Aguado, and P. San-Jose, Phys. Rev. B **96**, 085418 (2017).
[19] M.-T. Deng, S. Vaitiekėnas, E. Prada, P. San-Jose, J. Nygård, P. Krogstrup, R. Aguado, and C. M. Marcus, Phys. Rev. B **98**, 085125 (2018).
[20] F. Peñaranda, R. Aguado, P. San-Jose, and E. Prada, Phys. Rev. B **98**, 235406 (2018).
[21] J. Danon, A. B. Hellenes, E. B. Hansen, L. Casparis, A. P. Higginbotham, and K. Flensberg, Phys. Rev. Lett. **124**, 036801 (2020).
[22] G. C. Ménard, G. L. R. Anselmetti, E. A. Martinez, D. Puglia, F. K. Malinowski, J. S. Lee, S. Choi, M. Pendharkar, C. J. Palmstrøm, K. Flensberg, C. M. Marcus, L. Casparis, and A. P. Higginbotham, Phys. Rev. Lett. **124**, 036802 (2020).
[23] J. R. Tucker and M. J. Feldman, Rev. Mod. Phys. **57**, 1055 (1985).
[24] G. Platero and R. Aguado, Phys. Rep. **395**, 1 (2004).
[25] P. K. Tien and J. P. Gordon, Phys. Rev. **129**, 647 (1963).
[26] P. Kot, R. Drost, M. Uhl, J. Ankerhold, J. C. Cuevas, and C. R. Ast, Phys. Rev. B **101**, 134507 (2020).
[27] L. P. Kouwenhoven, S. Jauhar, K. McCormick, D. Dixon, P. L. McEuen, Y. V. Nazarov, N. C. van der Vaart, and C. T. Foxon, Phys. Rev. B **50**, 2019 (1994).
[28] Q.-F. Sun, J. Wang, and T.-H. Lin, Phys. Rev. B **58**, 13007 (1998).
[29] B. J. Keay, S. J. Allen, J. Galán, J. P. Kaminski, K. L. Campman, A. C. Gossard, U. Bhattacharya, and M. J. M. Rodwell, Phys. Rev. Lett. **75**, 4098 (1995).
[30] R. G. Mani, J. H. Smet, K. von Klitzing, V. Narayanamurti, W. B. Johnson, and V. Umansky, Nature (London) **420**, 646 (2002).
[31] M. A. Zudov, R. R. Du, L. N. Pfeiffer, and K. W. West, Phys. Rev. Lett. **90**, 046807 (2003).
[32] J. Shi and X. C. Xie, Phys. Rev. Lett. **91**, 086801 (2003).
[33] H.-Z. Tang, Y.-T. Zhang, and J.-J. Liu, AIP Adv. **5**, 127129 (2015).
[34] S. A. González, L. Melischek, O. Peters, K. Flensberg, K. J. Franke, and F. von Oppen, Phys. Rev. B **102**, 045413 (2020).
[35] D. T. Liu, J. Shabani, and A. Mitra, Phys. Rev. B **99**, 094303 (2019).
[36] Z. Yang, Q. Yang, J. Hu, and D. E. Liu, Phys. Rev. Lett. **126**, 086801 (2021).
[37] N. S. Wingreen, A.-P. Jauho, and Y. Meir, Phys. Rev. B **48**, 8487(R) (1993).
[38] Q.-F. Sun, J. Wang, and T.-H. Lin, Phys. Rev. B **59**, 13126 (1999).
[39] Q.-F. Sun and T.-H. Lin, J. Phys.: Condens. Matter **9**, 4875 (1997).
[40] B. Baran and T. Domański, Phys. Rev. B **100**, 085414 (2019).

[41] A.-P. Jauho, N. S. Wingreen, and Y. Meir, Phys. Rev. B **50**, 5528 (1994).
[42] G. Kells, D. Meidan, and P. W. Brouwer, Phys. Rev. B **86**, 100503(R) (2012).
[43] A. Vuik, B. Nijholt, A. R. Akhmerov, and M. Wimmer, SciPost Phys. **7**, 061 (2019).
[44] E. Prada, P. San-Jose, M. W. A. de Moor, A. Geresdi, E. J. H. Lee, J. Klinovaja, D. Loss, J. Nygård, R. Aguado, and L. P. Kouwenhoven, Nat. Rev. Phys. **2**, 575 (2020).
[45] C. O. Tabarner, Master's thesis, University of Copenhagen (2017).
[46] M. S. Rudner and N. H. Lindner, Nat. Rev. Phys. **2**, 229 (2020).
[47] S. Kohler, J. Lehmann, and P. Hänggi, Phys. Rep. **406**, 379 (2005).
[48] Y.-H. Li, J. Song, J. Liu, H. Jiang, Q.-F. Sun, and X. C. Xie, Phys. Rev. B **97**, 045423 (2018).
[49] J. C. Cuevas, A. Martín-Rodero, and A. Levy Yeyati, Phys. Rev. B **54**, 7366 (1996).
[50] S. Das Sarma, J. D. Sau, and T. D. Stanescu, Phys. Rev. B **86**, 220506(R) (2012).
[51] The fitting for square ratio of Bessel function may be multivalued. But we can avoid this ambiguity by considering a small field strength and $Q < 1$.
[52] M. Serina, D. Loss, and J. Klinovaja, Phys. Rev. B **98**, 035419 (2018).
[53] J. Wiedenmann, E. Bocquillon, R. S. Deacon, S. Hartinger, O. Herrmann, T. M. Klapwijk, L. Maier, C. Ames, C. Brüne, C. Gould, A. Oiwa, K. Ishibashi, S. Tarucha, H. Buhmann, and L. W. Molenkamp, Nat. Commun. **7**, 10303 (2016).
[54] O. Peters, N. Bogdanoff, S. Acero González, L. Melischek, J. R. Simon, G. Reecht, C. B. Winkelmann, F. von Oppen, and K. J. Franke, Nat. Phys. **16**, 1222 (2020).
[55] D. M. T. van Zanten, D. Sabonis, J. Suter, J. I. Väyrynen, T. Karzig, D. I. Pikulin, E. C. T. O'Farrell, D. Razmadze, K. D. Petersson, P. Krogstrup, and C. M. Marcus, Nat. Phys. **16**, 663 (2020).
[56] H. Pan and S. Das Sarma, Phys. Rev. Research **2**, 013377 (2020).
[57] C. Moore, T. D. Stanescu, and S. Tewari, Phys. Rev. B **97**, 165302 (2018).
[58] T. D. Stanescu and S. Tewari, Phys. Rev. B **100**, 155429 (2019).